Analysis and optimization of externally stiffened crush tubes

S. Salehghaffari, M. Rais-Rohani*, A Najafi

Department of Aerospace Engineering, Mississippi State University, Mississippi State, MS 39762, USA

A R T I C L E   I N F O

A B S T R A C T

Nonlinear finite element analysis is used to investigate the quasi-static axial collapse response of cylindrical tubes which are externally stiffened by multiple identical rings. The rings divide the long tube into a series of short thin-walled tubes. It is assumed that the size and shape of integral stiffeners are controlled through a machining process. The effects of various geometric parameters such as wall thickness, ring spacing, ring thickness and width on the collapse response, crush force and energy absorption of monolithic, integrally stiffened steel tubes are studied and used as a general framework for a design optimization study. Through design and analysis of computer experiments, global metamodels are developed for the mean crush force and energy absorption, using the radial basis function approximation technique. Using both single- and multi-objective design optimization formulations, optimum designs for different response characteristics are found. The crush mode in the form of progressive collapse or buckling is found to heavily depend on the ratio of stiffener spacing to stiffener height as well as the ratio of wall thickness to stiffener thickness. The optimization results show the viability of externally stiffened tubes as efficient energy absorbers.

1. Introduction

Energy absorption characterization of tubular components has been the subject of many experimental and theoretical studies [1–4]. Responses under both dynamic (crash) and quasi-static (crush) loads have been reported. Tube models found in the literature are fairly diverse in material (metallic or polymeric composite) and geometry, including circular, square and octagonal tubes [4–5] with single- and multi-cell configurations [6], tapered and s-shaped tubes and tube models that have honeycomb or foam-filled cavities [7,8]. Amongst them, circular tubes made of ductile materials have attracted much more attention, due to their plastic deformation, high stiffness- and strength-to-weight characteristics combined with an ease of manu-facturing. These tubes can dissipate an impact energy by various means, including plastic deformation, friction or tearing [5,9].

When a metallic tube is crashed into or crushed against a flat rigid wall, it undergoes an irreversible process whereby the crash/crush-induced energy is dissipated through plastic deformation or inelastic buckling. Generally, progressive plastic collapse with a stable mode of deformation (tube axis remains straight) offers a greater capacity for energy absorption than inelastic buckling that leads to an unstable response (local buckling and bending) with plastic deformation in only limited regions. As such, enhanced specific energy absorption (SEA, the ratio of total energy absorption to the tube mass) and stroke efficiency (SE, the ratio of deformed

length to the total tube length [3]) can be achieved by triggering the progressive collapse response.

Another means for energy dissipation is through the inversion mode of deformation when the tube is pressed against a rigid plug or die of certain shape, which causes the inward or outward folding (peeling or tearing) of the tube [10–14]. This mode occurs within the specific range of geometrical dimensions for the tube as well as the friction between the contacting surfaces. The low SE and strong sensitivity to external parameters, such as the loading condition, limit the viability of inversion mode as an energy absorption mechanism.

Axial splitting and curling of tubes against conical dies is also used as an energy absorption method [15–17]. In this failure mechanism, a large portion of tube length contributes to an energy dissipation (i.e., high SE), and the collapsing force is relatively steady. However, this method provides low crush load, and the crush performance is strongly affected by such external parameters as the loading direction.

Recently, plastic expansion of circular tubes by rigid inserts has been introduced as an efficient way to absorb energy without any serious sensitivity to loading direction and other external para-meters [18]. However, this method yields low SE and SEA values while it requires lower values of mean crush load to protect the structure from damage. The combination of different methods of energy dissipation (inversion and axial crushing of metal tubes in a single collapsible design) was investigated for the first time by Chirwa [19].

Among various methods of energy dissipation in crush tubes, progressive folding mechanism provides a relatively constant load and fairly high SE. In comparison to other energy dissipation

* Corresponding author. Tel.: +1 662 325 7294; fax: +1 662 325 7730.
E-mail address: masoud@ae.msstate.edu (M. Rais-Rohani).

methods, a greater percentage of tube material can contribute to plastic deformation providing high *SEA*. However, all of these favorable energy absorption characteristics can be achieved when the tube crushes progressively, and numerous experimental and theoretical studies [20–25] have shown that various parameters such as tube geometry, material properties, boundary conditions and loading conditions may affect the progressive crushing response.

Various design methods have been proposed to increase the SE and *SEA* of thin-walled tubes under axial crush loads. These investigations have also aimed to improve the stabilization of the collapse process and reduce the magnitude of peak load at the initial stage of the collapse. Abah et al. [26] investigated the effect of corner cutouts to initiate collapse and reduce the peak load of rectangular tubes under an axial load. Lee et al. [27] introduced triggering dents and investigated the effect of two types of dents, full- and half-dents, with the aim of decreasing the peak load. Shakeri et al. [28] introduced plastic buckling modes as an initial geometric imperfection in the post-buckling analysis to encourage progressive crushing and reduce maximum crush force in cylindrical tubes. Daneshi and Hosseinipour [29] showed that cutting circumferential grooves alternatively inside and outside of the tube at predetermined intervals could be an effective tool to force the plastic deformation to form at predetermined intervals along the tube. Using this pattern, it was possible to control the collapse shape of thin-walled structures. Singace and El-Sobky [30] investigated the energy absorption characteristics of corrugated tubes and showed that corrugations force plastic deformation to occur at predetermined intervals along the tube length and improve the uniformity of the load–displacement behavior of axially crushed tubes. Moreover the corrugated design of cylindrical tubes made it possible to predict and control the collapse mode in each corrugation, in order to optimize the energy absorption capacity of the tube.

Internal stiffening of metallic tubes with filler materials such as wood, metallic or non-metallic honeycomb and foam has also been shown to improve an energy absorption capacity in a number of investigations [31–33]. Non-compact crushing and global buckling behavior under axial loads are eliminated in the foam-filled tubes. Moreover in comparison with empty tubes of the same size, foam-filled tubes are less affected by loading parameters (i.e., direction and uniformity) and are more stable during the collapse process. By cutting a tube in several portions followed by the coaxial assembly, Abdul-Latif et al. [34] found that they could encourage the axisymmetric mode in an axial crushing of circular tubes.

Recently, Salehghaffari et al. [35] developed a new design concept to control energy absorption characteristics of thin-walled circular tubes under an axial compression. By machining wide circumferential grooves from the outer surface of a thick-walled tube at specific intervals, they arrived at a general design concept for an integrally stiffened (monolithic) tube, as shown in Fig. 1. The thicker portions (rings) essentially act as external stiffeners for the enclosed thin-walled tube sections. When the stiffened tube is subjected to an axial compression, the thin-walled sections between two adjacent ring stiffeners fold resulting in an enhanced energy absorption. This design model has been shown to be efficient in encouraging concertina folds, improving crushing stability, and making the component less sensitive to loading parameters, while improving its energy absorption characteristics such as an SE, maximum and mean crush forces and SEA.

Structural optimization techniques have been applied recently to optimize energy absorption characteristics of energy absorbing components. For an enhanced computational efficiency, surrogate models (metamodels) are often used in lieu of nonlinear finite element analysis (FEA) in structural design optimization studies. Response surface methodology (RSM) is among the commonly used metamodeling techniques used in crashworthiness optimization [36–38]. Yamazaki and Han [39], Lee [40] and Chiandussi et al. [41] have applied an RSM method in crashworthiness optimization of energy absorbing devices. However, the drawback of using second-order
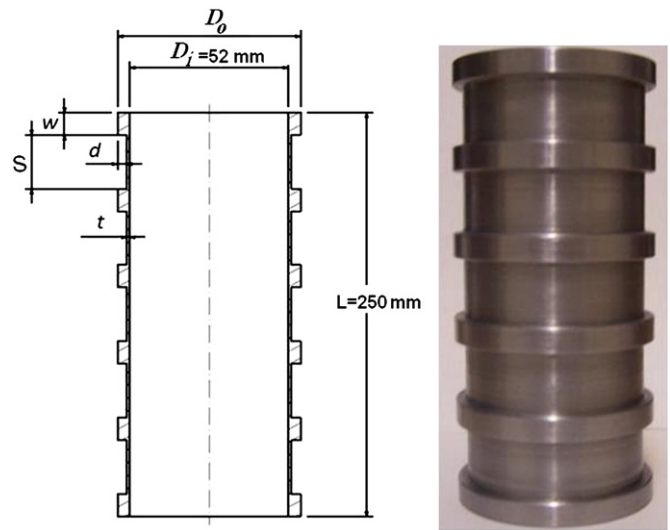

Fig. 1. Externally stiffened circular tube with associated geometric design parameters [35].

response surface (RS) models is that they may not be appropriate for creating global models that are accurate over the entire design space for highly nonlinear problems. Although it is possible to develop higher order RS models, they may not be effective or appropriate for crashworthiness optimization, partly due to the high computational cost in an extensive sampling of the design space [42]. Recent innovations to improve both the accuracy and efficiency of an RSM include the development and application of the sequential local RSM [43,44] adaptive RSM [45], and trust-region-based RSM [46]. These approaches partition the feasible design space into multiple small regions that can be accurately represented by low-order RS models.

In this paper, we present results of nonlinear finite element (FE) simulations of ring-stiffened tubes for various combinations of geometric parameters followed by shape and sizing optimization of such tubes for different choices of objective and constraint functions. Sampling of the design space is done using the Latin Hypercube Sampling (LHS) technique, while Radial Basis Functions (RBF) are used to build response metamodels that relate *SEA* and peak crush force to the geometric design variables associated with the externally stiffened tube model. Genetic algorithms (GA) are used as the optimizer for solving both constrained single- and multi-objective optimization problems.

2. Design and analysis of computer experiments

2.1. Description of an FE model

The basic geometry of the FE model, created according to the suggested guidelines [47], is shown in Fig. 2. The number of ring stiffeners in Fig. 1 is defined as an $N+1$, where N represents the number of thin-walled sections along the length of the tube. The stiffener section is defined by the geometric parameters d and w, whereas the thin-walled portions are defined by dimensions t and S. Hence, in the thick (stiffened) sections, total wall thickness is $t+d$. The tube's inner diameter $D_i = 52$ mm and length $L = 250$ mm are held fixed, while its other geometric parameters are allowed to vary in the optimization process as discussed later. It should be noted that S, w and N are related as

$$NS + (N+1)w = L \tag{1}$$

Through parameterization, the FE mesh can be readily updated for different combinations of design variables. A rigid plate, placed

at the bottom of the stiffened tube, is described as a moving rigid body with all degrees of freedom, except translation along the tube's axis set to zero. Also, all nodes at the top edge of the stiffened tube are constrained in all degrees of freedom.

We used the explicit finite element analysis (FEA) code LS-DYNA, version 971 to perform all nonlinear axial crush simulations. The quasi-static compression was simulated by moving the rigid plate with a constant upward velocity of 0.1 m/s. In order to reduce the time steps and computational time, the mass density of the tube material (steel) was scaled up 1000 times the original density. Thus, under this loading condition, no inertial or dynamic effects were present in the deformation process.

To define contact between the moving rigid plate and the stationary tube, "surface-to-surface" contact type was adopted with tube and plate nodes defined as "slave" and "master" nodes, respectively.
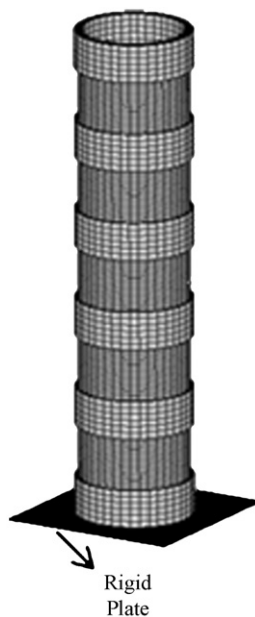

Fig. 2. FE model of the externally stiffened tube.

A "single-surface" interface was also selected to prevent penetration of the contacting elements in the tube model. The friction coefficient for surface-to-surface and single-surface contacts was set to 0.3 and 0.15, respectively.

We used solid (hex8) elements in all computer simulations. The sensitivity of the simulated results to mesh density for each computer experiment was analyzed in order to choose a suitable element size for the simulation. In some computer experiments, program termination due to the appearance of negative volume of solid elements was observed. This was caused mainly by the element Jacobian calculation at geometric points of the outer boundary of highly deformed solid elements [47]. In some computer experiments, rapid compression of elements in the stiffener sections as well as the nearby elements in the thin-walled sections resulted in an occurrence of a negative volume in solid elements. Through several computer simulations, it was discovered that the following factors contributed to the negative volume.

Element size: computational experiments indicated that highly deformed areas of the stiffened tube with smaller element size contribute to negative volume calculation. Hence, element size was increased from 1 × 1 (models without negative volume problem) to 2.3 × 2.3 (models with negative volume problem) to prevent this problem without sacrificing the solution accuracy. Therefore, suitable element size varies from 1 × 1 to 2.3 × 2.3 in different tube models. Note that an element size of 2.3 × 2.3 is found to be the closest element size to 1 × 1 that would help prevent the problem of negative volume, while maintaining the simulation accuracy.

Hourglass: deformation of solid elements in an hourglass mode can also result in the negative volume. Hence, we used hourglass control option in LS-DYNA simulations to resolve this problem. For hourglass control, we used Eq. (6) [47] in LS-DYNA with hourglass coefficient of 0.1, linear bulk velocity coefficient of 1.5 and quadratic bulk velocity coefficient of 0.06.

Interior contact setting: since solid elements in the thick regions of the tube have minimal participation in the plastic deformation, an interior contact setting was used to help alleviate the negative volume problem.

In the quasi-static simulations of the models in Table 1, we considered all of the factors mentioned above and took corrective actions to ensure the solution accuracy.

Table 1
Design points used in an RBF fitting.

Design #	N	d (mm)	t (mm)	S (mm)	w (mm)	Design #	N	d (mm)	t (mm)	S (mm)	w (mm)
1	5	1.91	1.93	27.08	19.10	25	3	0.51	2.37	75.00	6.25
2	5	2.15	1.26	43.75	5.21	26	3	0.93	1.57	45.00	28.75
3	5	1.55	2.53	32.29	14.76	27	3	2.17	1.46	60.00	17.5
4	5	2.88	2	36.46	11.28	28	3	1.76	2.49	69.00	10.75
5	5	2.28	1.07	31.25	15.63	29	3	1.55	1.8	63.00	15.25
6	5	2.03	1.73	44.79	4.34	30	3	1.14	1	54.00	22.00
7	5	0.46	2.2	38.54	9.54	31	3	1.96	1.91	78.00	4.00
8	5	0.58	2.33	26.04	19.97	32	3	2.79	1.8	42.00	31.00
9	5	2.4	1.2	47.92	1.74	33	3	0.31	1.23	57.00	19.75
10	5	0.95	1.8	29.17	17.36	34	3	1.34	2.14	51.00	24.25
11	5	0.7	2.47	42.71	6.08	35	7	0.51	1.46	29.86	5.13
12	5	1.67	1.67	34.37	13.02	36	7	1.55	2.37	26.00	8.50
13	5	1.19	2.13	33.33	13.89	37	7	2.17	1	22.14	11.88
14	5	2.76	2.4	45.83	3.47	38	7	2.79	2.14	27.29	7.38
15	5	1.43	1	41.67	6.94	39	7	1.96	1.57	19.57	14.13
16	5	0.34	1.47	48.96	0.87	40	7	2.59	1.69	33.71	1.75
17	5	1.07	1.6	46.88	2.60	41	7	1.55	1.8	26.00	8.50
18	5	2.64	2.07	25.00	20.83	42	7	0.93	1.91	31.14	4.00
19	5	0.22	1.13	28.13	18.23	43	7	0.1	1.34	23.43	10.75
20	5	1.79	1.40	40.65	7.81	44	7	1.76	1.23	32.43	2.88
21	5	1.55	1.80	37.50	10.42	45	7	1.14	2.26	18.29	15.25
22	5	2.52	1.33	35.42	12.15	46	7	0.31	1.80	17.00	16.38
23	5	0.83	2.27	30.21	16.49	47	7	0.72	2.49	28.57	6.25
24	3	2.59	2.57	66.00	13.00	48	7	2.38	2.03	20.86	13.00

The material in the FE model is treated as an elastic–plastic with the Young's modulus = 210 GPa, kinematic hardening (material model type 3 in LS-DYNA) and von Mises yield criterion specified. The true stress–true strain curve of seamless steel, obtained by a standard tensile test as shown in Fig. 3, was used to approximate the data points in the plastic region of curve for all numerical simulations. Also, the rigid movable plate was simulated using the material model type 20. All numerical simulations of design samples were performed on a Pentium PC 3.2 GHz with a typical simulation time of 6–8 h. Comparison of FE results of some samples with those of experiments [35] validated the accuracy of FE model predictions.

2.2. Basic mechanism of plastic collapse

In the recent articles by Salehghaffari et al. [48,49], the results of an in-depth theoretical and experimental investigation into the collapse mechanism of ring-stiffened circular tubes were presented. Assuming a uniform and stable crush response, the general mechanism for an energy absorption in ring-stiffened circular tubes is illustrated in Fig. 4. As the axial load is increased, the thin-walled segments supported by the ring stiffeners undergo plastic deformation that is dominated by the formation of three plastic hinges. The so-called concertina folds are generated in the thin-walled sections of the tube in a fairly sequential fashion. While stiffeners help stabilize the crushing process, they generally provide no contribution to plastic deformation and energy absorption. The only exception is in the cases where dimension d and/or w (Fig. 1) are/is reduced to the level that makes the stiffeners less rigid and susceptible to the lateral bending. Hence, SE, SEA and crush force are generally governed by the response of the thin-walled segments of the tube. Depending on the geometric properties of the tube, the crush response may become non-uniform resulting in reduced energy absorption capacity [48,49].

2.3. Generation of random samples

Based on our previous experience with an analysis of externally stiffened circular tubes [35,48,49], the optimization search is limited to design samples with 4, 6 and 8 stiffeners (i.e., $N+1=4$, 6 and 8). For generation of random samples, it is necessary to have bounds on individual design variables. Assuming $w=0$, it can be seen from Fig. 1 that the upper bound for S corresponds to $N_{min}=3$
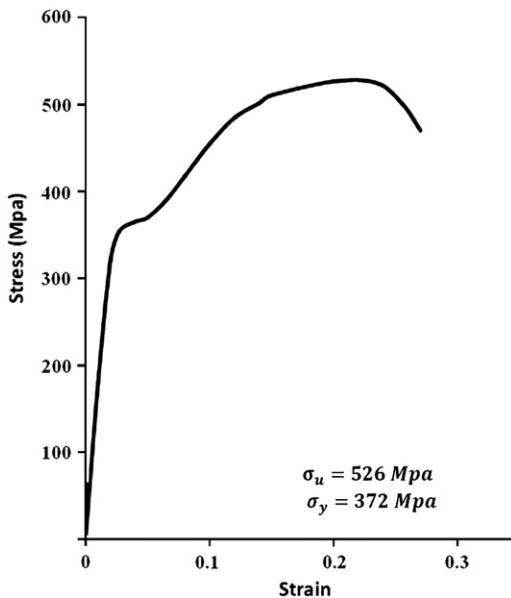
Fig. 3. True stress–true strain curve for seamless steel.
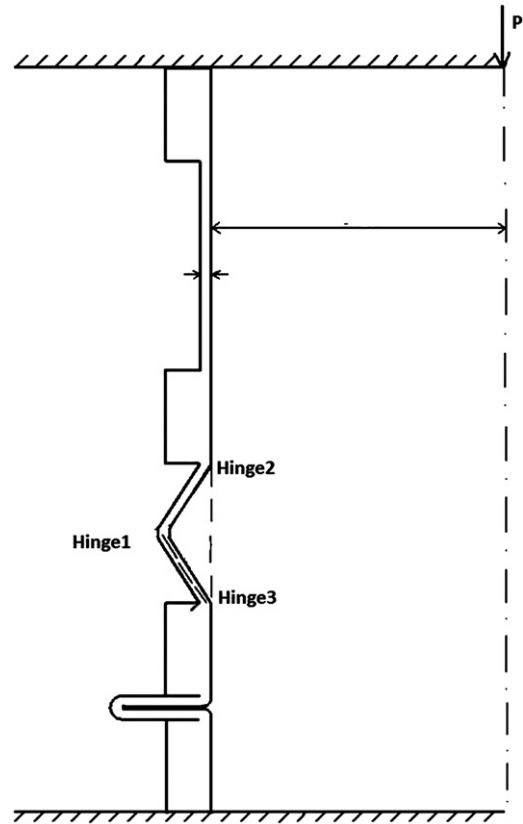
Fig. 4. Mechanism of plastic collapse in externally stiffened cylindrical tubes under an axial compression [48,49].

and is given by

$$S_{upper} = \frac{L}{N_{min}} = \frac{250}{3} = 83.3 \tag{2}$$

The thin-walled portions of the tube are the principal contributors to plastic deformation with potential length equal to $N \times S$. For SE = 0.5 (i.e., at least 50% of the tube length is crushed), we find the lower bound on an S as

$$S_{lower} = \frac{L}{2N_{max}} = \frac{250}{2 \times 7} = 17.85 \tag{3}$$

It is worth noting that the tube samples may have SE values slightly < 0.5 due to the fact that in the selected samples $w > 0$. Substituting Eqs. (2) and (3)b into Eq. (1), the bounds for w are found to be

$$w_{lower} = 0 \quad w_{upper} = \frac{L}{2(N_{min}+1)} = \frac{250}{2(3+1)} = 31.25 \tag{4}$$

Also, based on the previous observation of the effects of t and d on the plastic collapse mode and the corresponding mean crush force [35,48,49], the following bounds are imposed.

$$1 \leq t \leq 2.6 \quad 0 \leq d \leq 3 \tag{5}$$

Using an LHS technique and the selected bounds on the design variables, we examined 48 design points. In the sampling process, the random values for w and S for each design point were put into Eq. (1) to calculate N. If the N value was found to be a non-integer, it was modified to a number closest to 3, 5 or 7. In the second step, values of w and modified N were put into Eq. (1) to obtain the modified value of S for each sample. Geometric parameters of the randomly selected design samples with modified values of S are shown in Table 1. Among the 48 design-of-experiments (DOE)

samples, 11, 23 and 14 of them have 4, 6 and 8 stiffeners, respectively.

2.4. Simulation results and discussion

The simulation results for different tube samples are given in Table 2. They include the values for tube weight, SEA, maximum and average crush forces (P_{max}, P_{mean}), crush force efficiency (i.e., P_{mean}/P_{max}), stroke or crush length, stroke efficiency and an indication of crushing stability. Here, the crush length refers to the maximum distance traveled by the moving rigid plate at the bottom of the tube before an unstable crushing is observed in the simulation results. Stable crush mode refers to the progressive collapse along the tube axis, whereas an unstable mode involves buckling with or without the progressive collapse. In the latter case, a lateral rotation or bending of 10° in the tube axis is used as a criterion for identifying the mixed crush modes that are buckling dominated.

SEA is often used as an accurate measure of energy absorption capacity of the component [5]. On the other hand [3,5], an ideal energy-absorbing design should provide a desirable constant mean crush force–crush distance response under an axial loading. Generally, the initial peak in the crush–force–crush distance response represents the maximum crush force (P_{max}) that typically occurs soon after the start of the crush process and is due to the initial elastic resistance. While it is desirable to increase an SEA, it is preferable to decrease P_{max} in search of an optimum tube design. Moreover if tube remains fairly straight during the crush process, its energy absorption capacity will be enhanced.

Figs. 5 and 6 show the collapsed shapes separated by the mode shapes. While most ring-stiffened tube designs undergo stable crushing, others experience lateral bending resulting in crushing instability. It is worth noting that a prismatic circular tube with the same length-to-diameter ratio as the average among the stiffened tube models (i.e., 4.81) would experience global buckling at the initial stages of experiencing axial compression.

Numerical simulation of samples in Table 1 with different geometric properties reveals that it is possible to identify the tube characteristics that result in stable or unstable crush responses. Fig. 7(a) shows the plot of S/w versus $t/(d+t)$ and it indicates that

Table 2
FEA results for the randomly selected DOE design points.

| Design #	Weight (kg)	SEA (kJ/kg)	P_{max} (kN)	P_{mean} (kN)	Crush force efficiency	Stroke length (mm)	Stroke efficiency	Crushing stability
1	0.947	11.94	142.70	88.28	0.62	128.09	0.51	Stable
2	0.507	18.17	87.74	49.83	0.57	184.92	0.74	Stable
3	1.04	19.17	190.84	138.19	0.72	144.26	0.58	Stable
4	0.942	20.79	148.40	121.09	0.82	161.75	0.64	Stable
5	0.642	6.95	76.18	34.38	0.45	129.85	0.52	Stable
6	0.643	21.85	124.77	74.74	0.60	187.99	0.75	Stable
7	0.766	22.37	166.72	105.24	0.63	162.80	0.65	Stable
8	0.872	16.22	173.40	120.20	0.69	118.39	0.47	Stable
9	0.425	12.28	81.91	35.04	0.43	148.93	0.60	Unstable
10	0.730	10.11	128.92	69.28	0.54	106.59	0.43	Stable
11	0.859	18.60	188.98	115.74	0.61	138.02	0.55	Unstable
12	0.730	14.92	120.14	71.61	0.60	152.05	0.60	Stable
13	0.845	17.85	156.21	105.03	0.67	143.63	0.57	Stable
14	0.882	25.59	184.71	116.01	0.63	194.54	0.78	Unstable
15	0.405	18.00	68.60	39.61	0.58	184.00	0.74	Stable
16	0.483	20.16	103.69	54.20	0.52	179.67	0.72	Unstable
17	0.548	16.56	113.78	58.51	0.51	155.13	0.62	Unstable
18	1.160	7.05	151.42	80.6	0.53	101.48	0.41	Stable
19	0.400	10.08	70.36	33.49	0.48	120.37	0.48	Unstable
20	0.573	16.85	98.23	55.86	0.57	172.87	0.69	Stable
21	0.728	17.84	132.63	84.45	0.64	153.82	0.62	Stable
22	0.691	9.01	98.18	44.05	0.45	141.33	0.57	Stable
23	0.870	18.44	169.23	120.12	0.71	133.58	0.53	Stable
24	0.945	20.00	169.01	113.27	0.67	166.67	0.67	Stable
25	0.806	26.79	179.58	120.39	0.67	179.34	0.72	Stable
26	0.662	10.46	116.67	61.17	0.52	113.19	0.45	Stable
27	0.687	13.05	103.92	60.03	0.58	149.32	0.60	Stable
28	0.939	24.97	188.98	127.15	0.67	184.41	0.73	Stable
29	0.725	15.76	134.63	75.83	0.56	150.67	0.60	Stable
30	0.460	8.52	70.25	30.04	0.42	130.46	0.52	Stable
31	0.674	16.27	137.24	79.35	0.58	138.19	0.55	Unstable
32	1.087	6.71	129.73	70.32	0.54	103.66	0.41	Stable
33	0.433	10.73	83.22	38.82	0.47	119.71	0.47	Unstable
34	0.892	13.64	166.26	96.30	0.58	126.3	0.51	Stable
35	0.506	21.51	117.62	58.28	0.50	186.78	0.57	Stable
36	0.939	15.96	175.58	107.23	0.61	139.74	0.56	Stable
37	0.608	7.43	69.00	33.60	0.49	134.43	0.54	Stable
38	0.947	15.15	154.84	91.73	0.59	156.38	0.63	Stable
39	0.824	6.86	110.75	51.59	0.47	109.50	0.44	Stable
40	0.603	19.40	121.38	67.4	0.56	173.57	0.69	Unstable
41	0.740	15.11	130.05	73.00	0.56	153.12	0.61	Stable
42	0.672	24.69	137.82	87.89	0.64	188.74	0.75	Stable
43	0.449	14.56	116.5	51.17	0.44	127.73	0.51	Unstable
44	0.452	15.85	112.23	41.01	0.44	174.67	0.70	Unstable
45	0.947	13.26	170.98	123.20	0.72	101.95	0.41	Stable
46	0.648	16.29	132.25	79.39	0.60	132.93	0.53	Unstable
47	0.881	23.45	184.88	118.12	0.64	174.90	0.7	Stable
48	1.025	10.09	147.81	89.53	0.61	115.57	0.59	Stable
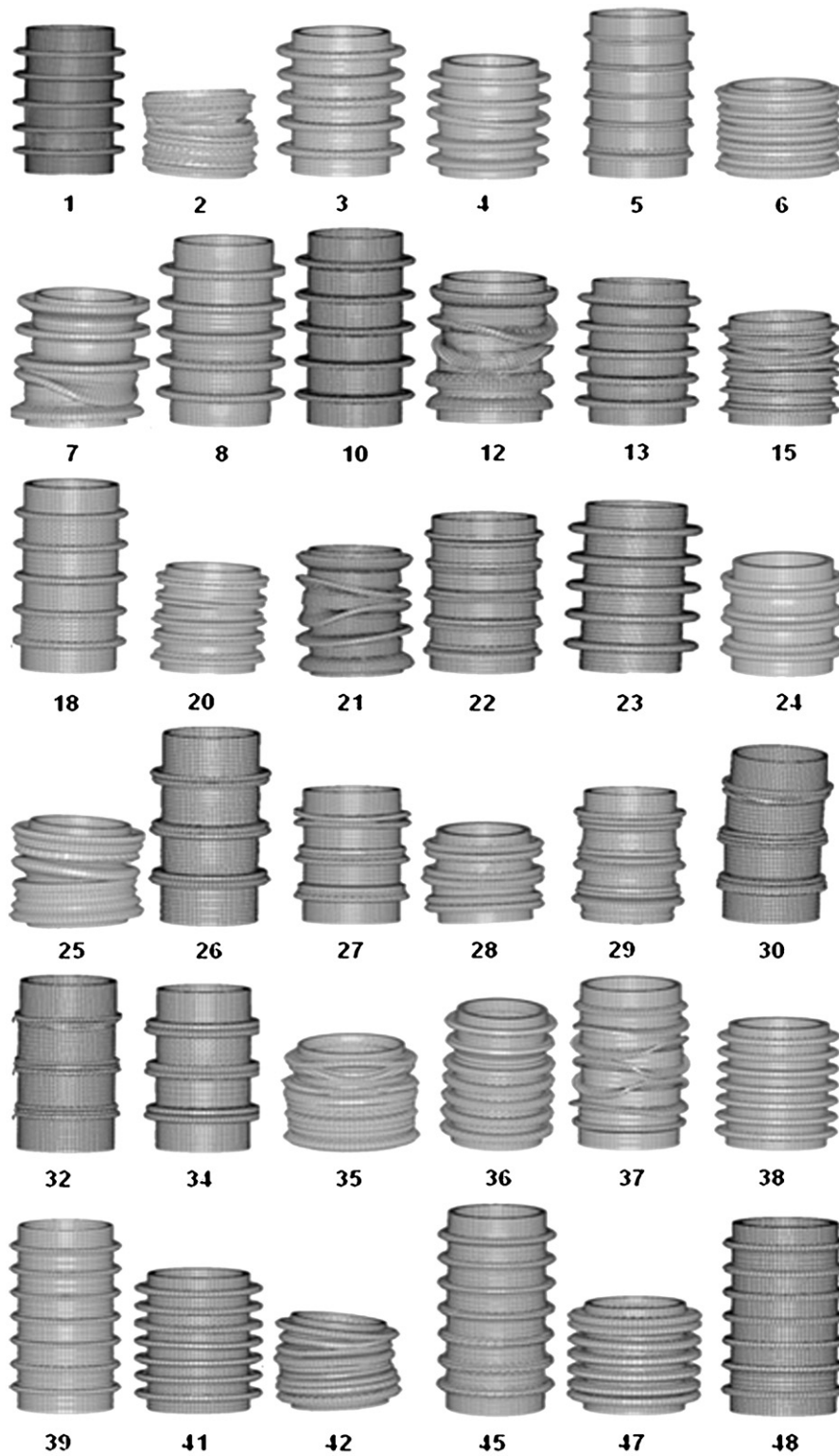
Fig. 5. Collapsed shapes of samples with stable deformation.

samples with $S/w < 12$ have a stable crush response for a wide range of $t/(d+t)$ values that extend from 0.3 to around 0.8. For samples with $S/w > 12$ or $t/(d+t) > 0.8$, lateral instability will occur. Fig. 7(b) shows the plot of S/t versus $w/(d+t)$. For $2 \leq w/(d+t) \leq 7$, the tube undergoes stable crush for all values of S/t considered. However, for $w/(d+t) < 2$, lateral instability will occur for any value

of S/t as noted in Fig. 7(b). For $w/(d+t) > 7$, it is possible to encounter both stable and unstable crush modes based on the value of S/t.

As also found in the previous research [35,48,49], it appears that while for large values of w and d the stiffened regions do not contribute to the plastic deformation, they play a significant role in stabilizing the crushing process. However, unnecessary selection of
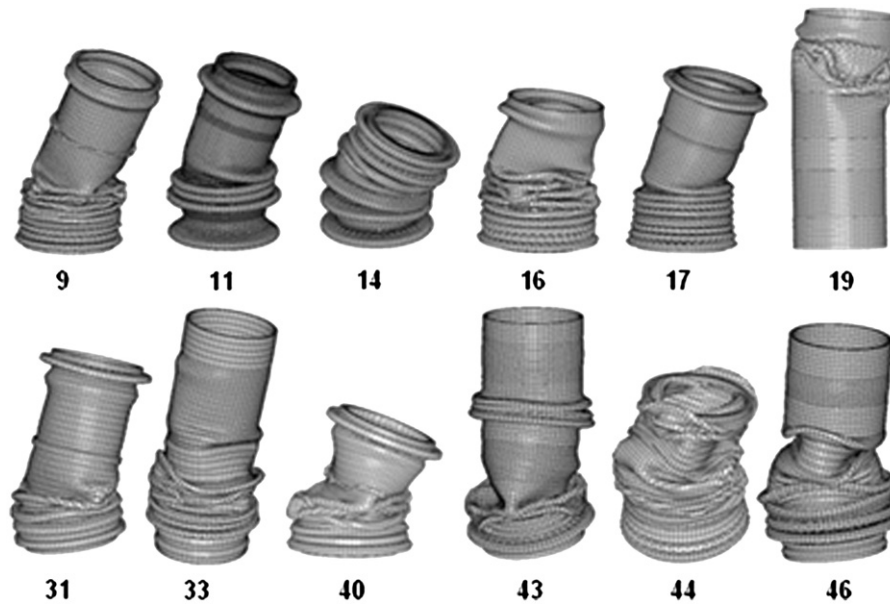
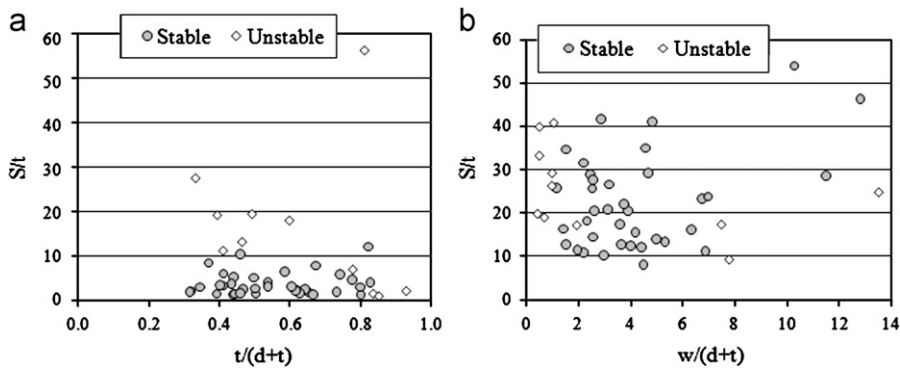**Fig. 6.** Collapsed shapes of samples with an unstable deformation.

Fig. 7. Geometric regions for stable and unstable crushing of stiffened tubes.

Table 3
Effect of decreasing parameter d on crush characteristics of design # 38.

Decreasing percentage of d	d/t	Stroke length (mm)	P_{mean} (kN)	P_{max} (kN)	Weight (kg)	SEA (kJ/kg)	Crushing stability
40	0.782	156.38	91.72	154.99	0.849	16.90	Stable
90	0.13	169.02	103.06	156.24	0.732	22.81	Stable
95	0.07	172.05	102.09	160.07	0.718	25.46	Unstable

large values for w and d increases the weight of the stiffened tube without providing any improvement in crushing stability or energy absorption.

Table 3 gives a summary of simulation results if d is decreased by 40%, 90% and 95%. Fig. 8 also shows the collapsed shape for each modified model. Decreasing d by as much as 40% does not affect the collapse mode, but it decreases the weight and improves an SEA of the stiffened tube. However, P_{mean}, P_{max} and SE are not affected by the 40% reduction in d (see Tables 2 and 3). Interestingly, decreasing d by as much as 90% or 95% not only improves the SEA value, but also leads to improvements in P_{mean} and SE. In these modifications, the stiffened portions become thin enough to deform plastically and contribute to an energy absorption. Also, Fig. 8 shows that decreasing d by 90% keeps the crush mode stable, whereas a 95%
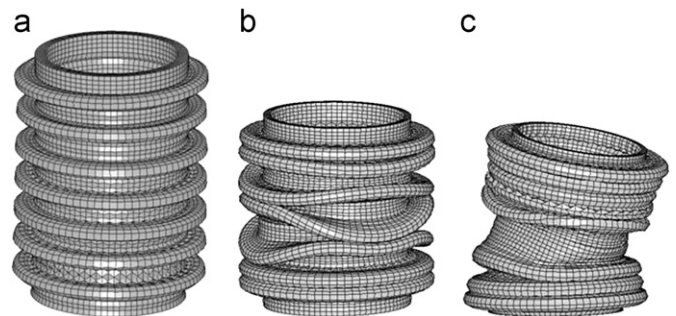

Fig. 8. Collapsed shape of design number 38 with d reduced by (a) 40%, (b) 90% and (c) 95%.

reduction results in an instability at the final stages of the crushing process. It is not surprising to see the crushing instability for the 95% case since the d/t ratio is very small. However, it still provides a better P_{mean} and SE than that of the case with 90% decrease. In fact, at very small values of d, external rings act more like a trigger mechanism than stiffeners.

Figs. 9 and 10 show the formation of the concertina folds between the adjacent ring stiffeners and the corresponding load–displacement curve for the sample 41, respectively. At the initial
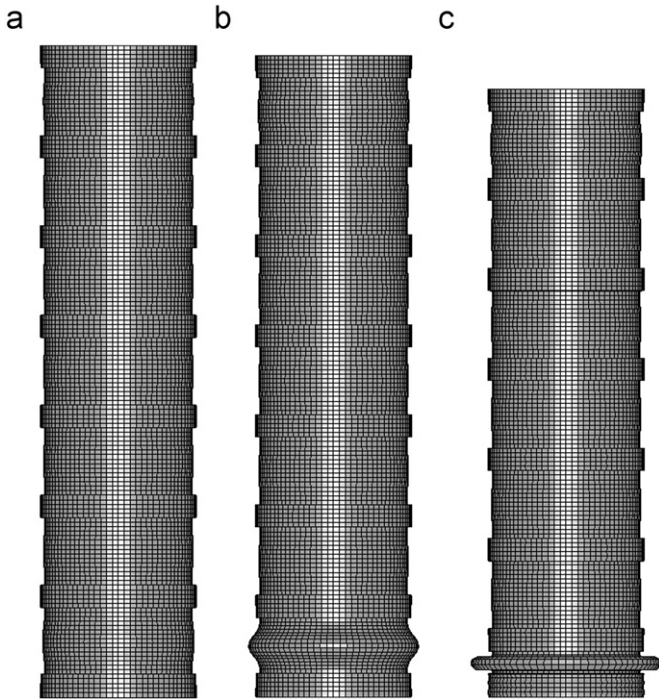
Fig. 9. Essential features in the formation of the first concertina fold between two adjacent ring stiffeners for sample 41 showing (a) local lateral deformation of all thin-walled sections, (b) initial formation of plastic hinges and (c) complete formation of a concertina fold.
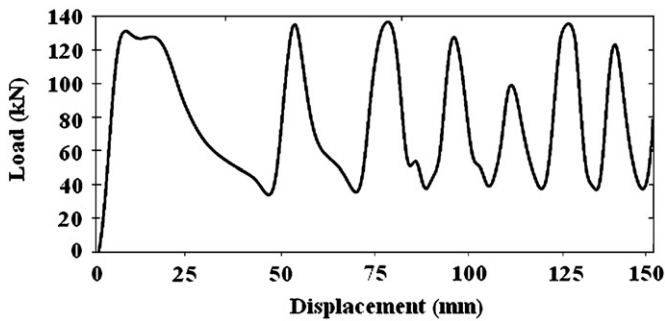

Fig. 10. Load–displacement curve for the sample 41.

stages of crush, the thin-walled sections begin to deform in the shape of a barrel with two stationary plastic hinges at the top and bottom edges along with a moving hinge line in the middle (see Fig. 4). Further compression causes the middle plastic hinge line in the bottom section to move outward in the radial direction until the top and bottom sides of the lobe come in contact (see Fig. 9). This phenomenon creates the first fluctuation of reaction load in Fig. 10. The same process happens in the formation of the subsequent concertina folds in the other thin-walled sections. However, the pressing plate travels a longer distance in the formation of the first concertina fold than the rest. This is due to the local deformation of all thin-walled sections at the initial stages of pressing the whole tube before the first concertina fold is formed. In fact, local deformation of all thin-walled sections at the initial stages of crushing is responsible for reducing the initial peak crush force significantly.

Final collapsed shapes of samples 7, 12, 21 and 37 (see Fig. 5) show that for some combination of stiffener dimensions and spacing, it is possible to encounter a combined mode of deformation that involves twisting, wrinkling and concertina folds. This trend was also observed in some experimental results [48,49]. Formation of more concertina folds within longer thin-walled sections is observed for some samples (see Fig. 5), while for others (e.g., 12 and 21) the thin-walled section is not long enough to allow the formation of two concertina folds. In these thin-walled sections, firstly, two stationary plastic hinges, one at top edge and the other at a long distance from the bottom edge, along with a moving plastic hinge at their mid distance are formed. Then, a concertina fold is shaped near the top edge of the thin-walled section. This is followed by compression of the rest of the material between the bottom edge and the formed concertina fold that causes the formation of wrinkles. Formation of diamond folds is observed in samples 2 and 35. This is because of the geometry of the thin-walled sections that is not appropriate for the formation of concertina folds.

3. Optimization problem description

The three principal factors we considered in the design optimization of ring-stiffened cylindrical crush tubes are energy absorption, weight and maximum crush force. Since an SEA represents the ratio of total energy absorption to the tube mass, it allows two of the factors to be represented by a single metric. Both single-objective constrained and multi-objective optimization problems are considered in this section in order to show the impact of the problem formulation on the optimization results.

The tube design problem can be modeled using two different single-objective constrained optimization problems. In the first model, the optimum values of the four geometric parameters in Fig. 1 are sought that would

$$\text{Maximize} \quad f_1 = SEA(X)$$
$$\text{s.t.} \quad P_{\max}(X) \le P_{\max}^C$$
$$X^L \le X \le X^U \tag{6a}$$

where $P_{\max}$ is the maximum crush force with an upper bound of $P_{\max}^C$. In the second model, we seek the optimum values of design variables that would

$$\text{Minimize} \quad f_2 = P_{\max}(X)$$
$$\text{s.t.} \quad SEA(X) \ge SEA^C$$
$$X^L \le X \le X^U \tag{6b}$$

where SEA^C is the lower bound on SEA and X represents the vector of design variables (i.e., $X^T = [w, S, d, t]$) with X^L and X^U as the corresponding lower and upper bounds, respectively.

In the multi-objective optimization problem, a compromise or Pareto optimum solution is sought with the goal of pushing towards the point of Utopia resulting in SEA maximization and $P_{\max}$ minimization. Several methods have been developed for the solution of multi-objective design optimization problems by searching for the non-dominated design points that form the Pareto frontier in the criterion space [50,51]. As an alternative, utility function, inverted utility function, global criterion, or the compromise programming method [52] may be used to combine two or more objectives into a single composite objective function. Based on the value of weight factor assigned to each objective, the designer's preference towards a particular point on the Pareto frontier is established. Using the compromise programming approach, the optimization problem would be defined as

$$\text{Minimize} \left\{ \left[\frac{\mu(f_1^W - f_1^T)}{(f_1 - f_1^T)} \right]^2 + \left[\frac{(1-\mu)(f_2 - f_2^T)}{(f_2^W - f_2^T)} \right]^2 \right\}^{0.5}$$
$$\text{s.t.} \quad \mu \in [0, 1] \text{ and } X^L \le X \le X^U \tag{7}$$

where the superscripts T and W denote the target and the worst values, respectively, for each objective function. In the absence of specific target and worst values for an objective, the extreme (best and

worst) single-objective optimization values may be used instead. In Eq. (7), μ is the weight factor for assigning different levels of importance to each objective function.

Using the geometrical average of efficiency coefficients [53] associated with the two objectives, we would find an alternative formulation for the multi-objective optimization problem that can be expressed as

$$Maximize \quad F_g = \sqrt{d_{SEA}d_P}$$
$$s.t. \quad X^L \leq X \leq X^U \tag{8}$$

where d_{SEA} and d_p are efficiency coefficients of SEA and P_{max}, respectively. To maximize SEA in Eq. (8), d_{SEA} is calculated in terms of the relative distance to its worst value as

$$d_{SEA} = \frac{f_1 - f_1^W}{f_1^T - f_1^W} \tag{9}$$

To minimize P_{max}, d_p is calculated as

$$d_p = 1 - \frac{f_2 - f_2^W}{f_2^T - f_2^W} \tag{10}$$

Hence, with changes in design variables, d_{SEA} and d_p can take any value in the interval [0,1]. When the overall efficiency function, F_g, reaches one, the corresponding objective function reaches the optimal solution, whereas $F_g = 0$ indicates the worst solution.

4. Surrogate modeling

Radial Basis Functions (RBF) [42,44,54] are used to establish surrogate models (metamodels) to represent the relationships between the individual objective functions (SEA and P_{max}) and the design variable vector $\boldsymbol{X}^T = [w, S, d, t]$ over the entire design space bounded by the side constraints. Given the design variable vector and response values at n arbitrary design (training) points, an RBF approximation of the response function $f(\boldsymbol{X})$ derived from an FE simulation ("exact" response) can be found as

$$\tilde{f}(\boldsymbol{Y}) = \sum_{i=1}^{n} \lambda_i \phi \left(\|\boldsymbol{Y} - \boldsymbol{Y}_i\| \right) \tag{11}$$

where $\boldsymbol{Y}$ is the vector of normalized design (input) variables with $\boldsymbol{Y}_i$ representing the normalized coordinates of the ith training point, $r_i = \|\boldsymbol{Y} - \boldsymbol{Y}_i\| = \sqrt{(\boldsymbol{Y} - \boldsymbol{Y}_i)^T(\boldsymbol{Y} - \boldsymbol{Y}_i)}$ is the Euclidean norm representing the radial distance from any arbitrary design point to the ith training point, ϕ is a radial symmetric basis function, and $\lambda_i, i = 1$ are the unknown interpolation coefficients. Eq. (11) represents a linear combination of a finite number of radial symmetric basis functions.

Commonly used RBF formulations include: thin-plate spline [$\phi(r) = r^2 \log(r)$], Gaussian [$\phi(r) = e^{\alpha r^2}$, $\alpha > 0$], multiquadric [$\phi(r) = \sqrt{r^2 + c^2}$] and inverse multiquadric[$\phi(r) = 1/\sqrt{r^2 + c^2}$]. With normalized input variables, r falls in the range of (0, 1) with $0 < c \leq 1$. The choice of basis function and tuning parameter c is problem specific.

Four error metrics are used for the assessment of metamodel accuracy. Since RBF is an interpolation model, six randomly selected design points (different from any of the training points) within the global bounds of each design variable are used as test points for the evaluation of R^2 and $RSME$ statistics defined as

$$R^2 = 1 - \frac{SSE}{SST} \tag{12}$$

$$RMSE = \sqrt{\frac{SSE}{m}} \tag{13}$$

Table 4
Error estimation of RBF models.

Design objectives	Method 1 (test points)		Method 2 (design points)	
	R^2	$RMSE$	$PRESS$	$R^2_{prediction}$
SEA	0.969	0.0699	201.23	0.8277
P_{max}	0.988	0.0407	1073.69	0.9354

where SSE (sum of square errors) and SST (total sum of squares) are calculated as

$$SSE = \sum_{j=1}^{m} \left[f_j - \tilde{f}_j \right]^2 \tag{14a}$$

$$SST = \sum_{j=1}^{m} \left[f_j - \bar{f}_j \right]^2 \tag{14b}$$

where m is the number of test points, f_j is the FEA-based response value at the jth test point, $\tilde{f}_j$ is the corresponding approximate value calculated by the RBF model, and $\bar{f}_j$ is the mean value of all $f_{j''}$, $j = 1, m$.

The other two error statistics considered are prediction error sum of squares ($PRESS$) and R^2 for prediction ($R^2_{prediction}$) at the training points calculated as

$$PRESS = \sum_{i=1}^{n-1} \left[f_j - \tilde{f}_{(1)} \right]^2 \tag{15}$$

$$R^2_{Prediction} = 1 - \frac{PRESS}{SST} \tag{16}$$

where $\tilde{f}_{(1)}$ is the predicted value at the ith training point, using the RBF model created by $(n-1)$ training points that exclude the ith point.

4.1. Evaluation of RBF model accuracy

For both design objectives (SEA and P_{max}), we checked different RBF models and found that multiquadric with $c = 0.001$ gives the most accurate metamodels. For the overall accuracy of each metamodel, the error metrics mentioned earlier are used.

For $PRESS$ and $R^2_{Prediction}$ error evaluations, we checked the predictability of responses derived from constructed RBF models for 47 design points. Although a large number of training points is used for construction of each RBF metamodel, it is possible for some of the error metrics to provide unreliable predictions. For example, Fang and Want [55] have shown that for some responses, the error predictions based on $PRESS$ and $R^2_{Prediction}$ may not provide accurate error estimates for RBF models. For R^2 and RMSE error evaluations, 6 out of the 48 initial design points (i.e., 5, 10, 15, 20, 30 and 40) are selected as test points with the remaining 42 treated as training points for the calculation of coefficients, λ_i.

The error estimates are given in Table 4. As it can be seen, large values for R^2 and $R^2_{Prediction}$ and small values for RMSE and PRESS indicate reasonable accuracy of the constructed RBF surrogate models for both design objectives.

To validate the metamodel-based optimization results, FE simulations of the optimum designs will be performed to determine the true error in the response predictions.

5. Design optimization results

Due to the availability of analytical surrogate models for SEA and P_{max} and a relative small set of design variables, we used Genetic Algorithms (GA in Global Optimization toolbox of MATLAB) to

setup and solve all optimization problems. A stochastic search approach such as GA offers a viable strategy to explore different regions of the design space in search of the global optimum design point. First, a random population of 20 design points is selected based on the specified bounds on the design variables. The scattered cross-over fraction is set at 0.8, and constraint dependent option is adopted for the mutation function.

For linearly constrained optimization problems, the GA solver in MATLAB identifies active linear constraints and bounds to generate search directions, or mutants for the GA. For non-linearly constrained optimization problems, it formulates a subproblem subject to linear constraints and bounds, using penalty and Lagrange parameters. Once an approximate solution to the subproblem is found, the penalty and Lagrange parameters are updated for a new subproblem, and the solution process continues until convergence at a specified accuracy is reached.

Here, the solution of constrained single-objective and unconstrained multi-objective optimization cases for a specific weight factor (Eq. (7)) required 6 and 53 iterations, respectively, with each iteration of the constrained single-objective problem taking considerably more time than the unconstrained multi-objective optimization problem.

5.1. Constrained single-objective optimization

SEA and P_{max} are the main competing criteria affecting the design of stiffened crush tubes. With the lower and upper bounds on each design variable defined, Eq. (6) can be used to formulate two separate but related single-objective constrained optimization problems formulated as

$$\begin{aligned}
\text{Maximize} \quad & f_1 = \text{SEA}(S, w, t, d) \\
\text{s.t.} \quad & P_{max}(S, w, t, d) \leq 145\,kN \\
& 17.85\,mm \leq S \leq 83.3\,mm \\
& 0\,mm \leq w \leq 31.25\,mm \\
& 0\,mm \leq d \leq 3\,mm \\
& 1\,mm \leq t \leq 2.6\,mm
\end{aligned} \tag{17}$$

$$\begin{aligned}
\text{Minimize} \quad & f_2 = P_{max}(S, w, t, d) \\
\text{s.t.} \quad & \text{SEA}(S, w, t, d) \geq 24\,kJ/kg \\
& 17.85\,mm \leq S \leq 83.3\,mm \\
& 0\,mm \leq w \leq 31.25\,mm \\
& 0\,mm \leq d \leq 3\,mm \\
& 1\,mm \leq t \leq 2.6\,mm
\end{aligned} \tag{18}$$

The constraint bounds for P_{max} in Eq. (17) and SEA in Eq. (18) are based on the desire to have large values for SEA and moderate values for P_{max}. Therefore, we selected the bounds for P_{max} at 75% and SEA at 90% of the corresponding maximum values in Table 2, respectively. Eqs. (17) and (18) are solved for three different values of N (i.e., 3, 5 and 7).

In MATLAB, the established RBF surrogate models relating P_{max} and SEA to design the variable vector are placed in separate M-files to account for the presence of design constraints in the optimization problem described in Eqs. (17) and (18), respectively. The solutions for these optimization problems are given in Tables 5 and 6. With

Table 5
Maximization of SEA with constraint on $P_{max} \leq 145$ kN.

Optimal design variables				SEA (kJ/kg)	P_{max} (kN)
N	d (mm)	t (mm)	S (mm)	w (mm)		
7	0.927	1.916	31.178	3.969	24.693	138.005

Table 6
Minimization of P_{max} with constraint on SEA ≥ 24 kJ/kg.

Optimal design variables				SEA (kJ/kg)	P_{max} (kN)
N	d (mm)	t (mm)	S (mm)	w (mm)		
7	0.942	1.869	31.178	3.969	24.693	138.005

consistent constraint bounds, the solutions are nearly identical. The only minor difference is in the values of d and t. The larger number of stiffeners ($N+1=8$) enhances the structural characteristics of the stiffened tube. It should be noted that the wall thickness in the stiffened regions is $d+t$.

5.2. Multi-objective optimization using compromise programming method

Multi-objective optimization problem accounts for the interaction between competing design criteria [52] in search of Pareto optimal solutions. Using the compromise programming method, the multi-objective optimization problem is expressed as

$$\begin{aligned}
\text{Minimize} \quad & \left\{ \left[\frac{\mu \text{SEA}^*}{\text{SEA}(S, w, t, d)} \right]^2 + \left[\frac{(1-\mu)P_{max}(S, w, t, d)}{P^*} \right]^2 \right\}^{0.5} \\
\text{s.t.} \quad & \mu \in [0, 1] \\
& 17.85\,mm \leq S \leq 83.3\,mm \\
& 0\,mm \leq w \leq 31.25\,mm \\
& 0\,mm \leq d \leq 3\,mm \\
& 1\,mm \leq t \leq 2.6\,mm
\end{aligned} \tag{19}$$

where SEA^* and P^* are the normalization values for SEA and P_{max}, respectively. Different combination of weight factors in Eq. (19) gives different optimum design points on the Pareto frontier in the criterion space. The weight factor is varied in the range 0–1 at 0.1 increments resulting in the Pareto frontier shown in Fig. 11. Note that based on the formulation of Eq. (19), $\text{SEA}^*/\text{SEA}(S, w, t, d)$ is minimized for maximizing $\text{SEA}(S, w, t, d)$. The merit of Pareto set is that it provides a range of optimal solutions depending on the level of preference designer places on different objectives.

The results for different optimization problems and solution techniques are shown in Fig. 11. Of the eleven points corresponding to the solution of Eq. (19) with varying weight factor, some give very close answers and are not distinguishable in the figure. The solutions for Eqs. (17) and (18) overlap in the criterion space. The location of the multi-objective optimum point corresponding to Eq. (19) and $\mu = 0.4$ (details summarized in Table 7) is also shown. For comparison, the GA based multi-objective optimization solver of Matlab is also used to generate the Pareto frontier points marked as MOGA in Fig. 11. The results from Eq. (19) are found to be in very good agreement with those corresponding to MOGA.

5.3. Multi-objective optimization using geometrical average method

The multi-objective optimization problem is formulated as

$$\begin{aligned}
\text{Maximize} \quad & F_g(S, w, t, d) = \sqrt{d_{SEA} d_P} \\
\text{s.t.} \quad & 17.85\,mm \leq S \leq 83.3\,mm \\
& 0\,mm \leq w \leq 31.25\,mm \\
& 0\,mm \leq d \leq 3\,mm \\
& 1\,mm \leq t \leq 2.6\,mm
\end{aligned} \tag{20}$$

$$d_{SEA} = \frac{\text{SEA}(S, w, t, d) - \text{SEA}^L}{\text{SEA}^U - \text{SEA}^L} \tag{21}$$
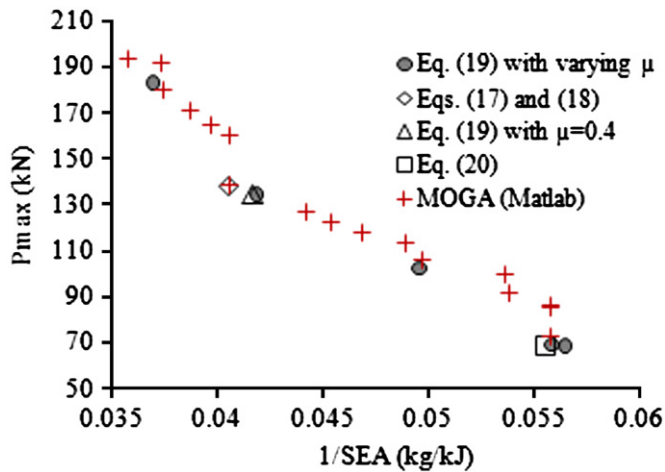
Fig. 11. Comparison of results for different optimization problems and solution techniques.

Table 7
Multi-objective minimization results using compromise programming with $\mu = 0.4$.

Optimal design variables				SEA (kJ/kg)	P_{max}(kN)
N	d (mm)	t (mm)	S (mm)	w (mm)		
7	0.864	1.836	32.210	3.060	23.9	134.3

Table 8
Multi-objective optimization results using the geometrical average method.

Optimal design variables				SEA (kJ/kg)	P_{max} (kN)	F_g	d_{SEA}	d_p
N	d (mm)	t (mm)	S (mm)	w (mm)					
5	1.428	1.001	41.713	6.906	18.000	68.720	0.656	0.672	0.640

$$d_p = 1 - \frac{P_{max}(S, w, t, d) - P^L}{P^U - P^L} \qquad (22)$$

where SEA^U, SEA^L and P^U, P^L represent the upper and lower bounds on SEA and P_{max}, respectively. The ideal values of efficiency coefficients (d_{SEA}, d_p) and overall cost function, $F_g(S, w, t, d)$, are 1.

The results for this problem are summarized in Table 8 with the corresponding optimum point shown in Fig. 11. It can be seen that the optimization result of geometrical average method corresponds to a specific point on the Pareto frontier. As Table 8 shows, the values for d_{SEA} and d_p are nearly the same, indicating that the optimal solution does not strongly favor one objective over the other. However, the method does not give the same solution as the constrained single-objective optimization problem. The optimum value for N is also different than those found in the other optimization problems.

5.4. Verification of optimum design with FE simulations

Estimated optimal values of *SEA* and P_{max} derived from solutions of Eqs. (17), (19) (using weight factor of 0.4) and Eq. (20), using RBF surrogate models given in Table 9. The corresponding exact values found from FE simulations are also given in Table 9 to measure the accuracy of RBF based designs. The optimization results are found to have reasonably good accuracy with slight over- or under-predictions of the estimated responses, as indicated by a maximum error of approximately 5% in *SEA* and 1.6% in P_{max} predictions.

Table 9
Comparison of RBF predicted optima with FEA simulation results.

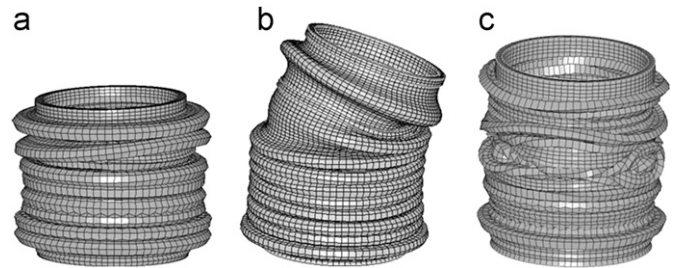| Solution for Eq. #	SEA (kJ/kg)			P_{max} (kN)		
	RBF	FEA	% Error	RBF	FEA	% Error
17	24.693	24.996	1.21	138.005	138.060	0.040
19	23.900	23.330	2.44	134.300	132.210	1.581
20	18.000	17.131	5.07	68.720	68.622	0.143

Fig. 12. Crush pattern of an optimal model found from (a) Eq. (17), (b) Eq. (19) with weight factor of 0.4 and (c) Eq. (20).

Collapsed shapes of optimized stiffened tubes are shown in Fig. 12. It appears that the solutions from Eqs. (17), (19) and (20) result in different collapse modes of deformation. Whereas the deformation response in Fig. 12(a) is fairly uniform; we see some lateral bending towards the final stages of the collapse in Fig. 12(b) and mixed wrinkling, twisting and concertina folds in Fig. 12(c).

6. Conclusion

The quasi-static axial collapse response of circular tubes with externally machined stiffeners was investigated using an explicit nonlinear finite element analysis. The size and spacing of the ring stiffeners were found to play an important role in determining the crush mode as well as the specific energy absorption and the peak crush force of the stiffened tube. The addition of external stiffeners is effective in changing the crush mode from global buckling to progressive plastic collapse.

Through design and analysis of computer experiments, separate surrogate models were developed using an RBF approximation. Both single- and multi-objective optimization problem formulations were used to find an optimal geometric design that results in maximum specific energy absorption and minimum peak crush force. The results show that the externally stiffened circular tubes are considerably more efficient than a prismatic circular tube in terms of energy absorption, stroke efficiency and structural weight.

References

[1] Abramowicz W, Jones N. Dynamic axial crushing of square tubes. Int J Impact Eng 1984;2:179–208.
[2] Abramowicz W, Jones N. Transition from initial global bending to progressive buckling of tubes loaded statically and dynamically. Int J Impact Eng 1997;19:415–37.
[3] Jones N. Structural impact. Cambridge, UK: Cambridge Press; 1989.

[4] Wierzbicki T, Abramowicz W. On the crushing mechanics of thin walled structures. J Appl Mech 1983;50:727–34.
[5] Alghamdi AAA. Collapsible impact energy absorbers: an overview. Thin-Walled Struct 2001;39:189–213.
[6] Najafi A, Rais-Rohani M. Influence of cross-sectional geometry on crush characteristics of multi-cell prismatic columns. In: Proceedings of the 49th AIAA/ASME/ASCE/AHS/ASC structures, structural dynamics and materials conference. 2008.
[7] Chen W, Wierzbicki T. Relative merits of single-cell, multi-cell and foam-filled thin-walled structures in energy absorption. Thin-Walled Struct 2001;39:287–306.
[8] Kim HS, Chen W, Wierzbicki T. Weight and crash optimization of foam-filled three-dimensional "S" frame. Comput Mech 2002;28:417–24.
[9] Johnson W, Reid SR. Metallic energy dissipating systems. Appl Mech Rev 1978;31:277–88.
[10] Al-Hassani STS, Johnson W, Lowe WT. Characteristics of inversion tube under axial loading. Int J Mech Sci 1972;14:370–81.
[11] Colokoglu A, Reddy TY. Strain rate and inertial effects in free external inversion of tubes. Int J Crashworthiness 1996;1:93–106.
[12] Kinkead AN. Analysis for inversion load and energy absorption of a circular tube. Int J Strain Anal 1983;18:177–88.
[13] Reddy TY. Tube inversion an experiment in plasticity. Int J Mech Eng Educ 1989;17:277–91.
[14] Reid SR, Harrigan JJ. Transient effects in the quasi static and dynamic inversion and nosing of metal tubes. Int J Mech Sci 1998;40:263–80.
[15] Huang X, Lu G, Yu TX. On the axial splitting and curling of circular metal tubes. Int J Mech Sci 2002;44:2369–91.
[16] Stronge WJ, Yu TX, Johnson W. Long stroke energy dissipation in splitting tubes. Int J Mech Sci 1983;25:637–47.
[17] Reddy TY, Reid SR. Axial splitting of circular metal tubes. Int Mech Sci 1986;28:111–31.
[18] Shakeri M, Salehghaffari S, Mirzaeifar R. Expansion of circular tubes by rigid tubes as impact energy absorbers: experimental and theoretical investigation. Int J Crashworthiness 2007;12:493–501.
[19] Chirwa EC. Theoretical analysis of tapered thin-walled metal inverbucktube. Int J Mech Sci 1993;35:325–51.
[20] Al Galib D, Limam A. Experimental and numerical investigation of static and dynamic axial crushing of circular tubes. Thin-Walled Struct 2004;42:1103–37.
[21] Andrews KRF, England GL, Ghani E. Classification of axial collapse of cylinder tubes under quasi-static loading. Int J Mech Sci 1983;25:687–96.
[22] Guillow SR, Lu G, Grzebieta RH. Quasi-static compression of thin-walled circular aluminum tubes. Int J Mech Sci 2001;43:2103–23.
[23] Hsu SS, Jones N. Quasi-static and dynamic axial crushing of thin-walled circular stainless steel, mild steel and aluminum alloy tubes. Int J Crashworthiness 2004;9:195–217.
[24] Karagiozova D, Jones N. Dynamic elastic–plastic buckling of circular cylindrical shells under axial impact. Int J Solids Struct 2000;37:2005–34.
[25] Murase K, Wada H. Numerical study on the transition of plastic buckling modes for circular tubes subjected to an axial impact load. Int J Impact Eng 2004;30:1131–46.
[26] Abah L, Limam A, Dejeammes M. Effects of cutouts on static and dynamic behavior of square aluminum extrusions. In: Proceedings of the Fifth international conference on structures under shock and impact, (SUSI V). Computational Mechanics, Southampton, UK; (1998). p. 133–42.
[27] Lee S, Hahn C, Rhee M, Oh JE. Effect of triggering on the energy absorption capacity of axially compressed aluminium tubes. Mater Des 1999;20:31–40.
[28] Shakeri M, Mirzaeifar R, Salehghaffari S. New insights into the collapsing of cylindrical thin-walled tubes under axial impact load. In: Proc Int Mech Eng Part C: J Mech Eng Sci 2007;221:869–85.
[29] Daneshi GH, Hosseinipour SJ. Grooves effect on crashworthiness characteristics of thin-walled tubes under axial compression. J Mater Des 2003;23:611–7.
[30] Singace AA, El-Sobky H. Behavior of axially crushed corrugated tubes. Int J Mech Sci 1997;39:249–68.
[31] Hanssen AG, Langseth M, Hopperstad OS. Static and dynamic crushing of circular aluminum extrusions with aluminum foam filler. Int Impact Eng 2000;24:475–507.
[32] Santosa S, Wierzbicki T. Crash behavior of columns filled with aluminum honeycomb or foam. Comput Struct 1998;68:343–67.
[33] Kim HS, Chen W, Wierzbicki T. Weight and crash optimization of foam-filled three-dimensional "S" frame. Comput Mech 2002;28:417–24.
[34] Abdul-Latif A, Baleh R, Aboura Z. Some improvements on the energy absorbed in axial plastic collapse of hollow cylinders. Int J Solids Struct 2006;43:1543–60.
[35] Salehghaffari S, Tajdari M, Panahi M, Mokhtarnezhad F. Attempts to improve energy absorption characteristics of circular metal tubes subjected to axial loading. Thin-Walled Struct 2010;48:379–90.
[36] Hou S-J, Li Q, Long S-Y, Yang X-J, Li W. Design optimization of regular hexagonal thin-walled columns with crashworthiness criteria. Finite Elem Anal Des 2007;43:555–65.
[37] Xiang Y-J, Wang Q, Fan Z-J, fang H-B. Optimal crashworthiness design of a spot-welded thin-walled hat section. Finite Elem Anal Des 2006;42:846–55.
[38] Acar E, Rais-Rohani M. Ensemble of metamodels with optimized weight factors. Struct Multidisciplinary Optim 2008;37:279–94.
[39] Yamazaki K, Han J. Maximization of the crushing energy absorption of cylindrical shells. Adv Eng Software 2000;31:425–34.
[40] Lee TH, Lee K. Multi-criteria shape optimization of a funnel in cathode ray tubes using a response surface model. Struct Multidisciplinary Optim 2005;29:374–81.
[41] Chiandussi G, Avalle M. Maximisation of the crushing performance of a tubular device by shape optimization. Comput Struct 2002;80:2425–32.
[42] Fang H, Rais-Rohani M, Liu Z, Horstemeyer M. A comparative study of metamodeling methods for multiobjective crashworthiness optimization. Comput Struct 2005;83:2121–36.
[43] Alexandrov NM, Dennis JE, Lewis RM, Torczon VA. Trust region framework for managing the use of approximation models in optimization. Struct Multi-disciplinary Optim 1998;15:16–23.
[44] Rais-Rohani M, Singh MN. Comparison of global and local response surface techniques in reliability-based optimization of composite structures. Struct Multidisciplinary Optim 2003;26:333–45.
[45] Wang G, Dong Z, Aitchison P. Adaptive response surface method—a global optimization scheme for approximation based design problems. J Eng Optim 2001;33:707–34.
[46] Rodriguez J, Renaud JE, Watson.LT. Trust region augmented Lagrangian methods for sequential response surface approximation and optimization. In: Proceedings of the DETC_97 ASME design engineering technical conference. Sacramento, CA: Paper no. DETC97/DAC3773, ASME. 1997.
[47] Hallquist JO, LS-DYNA 3D: theoretical manual, livermore software technology corporation. Livermore,1993.
[48] Salehghaffari S, Tajdari M, Mokhtarnezhad F. Collapse of thick-walled metal tubes with wide external grooves as controllable energy-dissipating devices. In: Proceedings of the international mechanical engineering, part C: J Mech Eng Sci 223 (2010). p. 2465–80.
[49] Mokhtarnezhad F, Salehghaffari S, Tajdari M. Improving the crashworthiness characteristics of cylindrical tubes subjected to axial compression by cutting wide grooves from their outer surface. Int J Crashworthiness 2009;14:601–11.
[50] Messac A. Physical programming: effective optimization for computational design. AIAA J 1996;34:149–58.
[51] Martinez MP, Messac A, Rais-Rohani M. Manufacturability-based optimization of aircraft structures using physical programming. AIAA J 2001;39:517–42.
[52] Rao SS. Engineering optimization theory and practice. 3rd ed.. John Wiley & Sons; 1996.
[53] Shujuan H, Qing L, Shuyao L, Xujing Y, Wei L. Crashworthiness design for foam filled thin-wall structures. Mater Des 2009;30:2024–32.
[54] Hardy RL. Multiquadratic equations of topography and other irregular surfaces. J Geophys 1971;76:1905–15.
[55] Fang H, Wang Q. On the effectiveness of assessing model accuracy at design points for radial basis functions. Commun Numer Methods Eng 2008;24:219–35.